High Entropy Alloys: Assessing Atomic-Scale Mixing and Surface Passivation with Time-of-Flight Secondary Ion Mass Spectrometry

Oscar F. Laurent,[1] Maria De Marco,[2] Marco Faustini,[2,3] Cédric Boissière,[2] Claude Poleunis,[1] Arnaud Delcorte[1,*], Damien P. Debecker[1,*]

[1] Université catholique de Louvain (UCLouvain), Institute of Condensed Matter and Nanosciences (IMCN), Place Louis Pasteur 1, Louvain-la-Neuve, 1348, Belgium

[2] Laboratoire Chimie de la Matière Condensée de Paris (LCMCP), Sorbonne Université–CNRS, 4, Place Jussieu, 75005 Paris, France

[3] Institut Universitaire de France (IUF), 75231 Paris, France

ToF-SIMS, porous high entropy alloy, aerosol, mixing, resistance to oxidation, catalysis

ABSTRACT: High entropy alloys (HEAs) are alloys that consist of five or more principal elements in near-equiatomic proportions, that tend to form simple solid solutions during solidification owing to high mixing entropy. HEAs have been identified as promising candidates for various heterogeneous catalysis and electrocatalysis applications. This work illustrates the utility of time-of-flight secondary ion mass spectrometry (ToF-SIMS) in analyzing HEAs, offering detailed chemical information about the top layers of a sample. Ru-Pt-Pd-Ir-Rh based porous HEAs with different mixing characteristics were analyzed alongside seven simpler alloys. An automatic quantification process was developed to effectively deal with the large data sets obtained from ToF-SIMS spectra of HEAs, allowing for accurate and reliable data interpretation. The complex chemical fingerprint obtained from the alloys surface was translated into a matrix showing the individual isotopic mass distributions of each poly atomic chemical species. From this, we introduce two key metrics: the Cluster Ratio (CR) and the Oxide Ratio (OR), to quantify respectively the degree of atomic-level mixing and the surface oxidation. With such data processing framework in hands, ToF-SIMS becomes a highly effective tool for assessing the properties of HEAs. Our findings reveal that increasing elemental complexity (number of different elements in the alloy) enhances atomic mixing. Moreover, HEAs with enhanced atomic mixing are shown to be more resistant to surface oxidation.

INTRODUCTION

High entropy alloys (HEAs) are alloys that consist of five or more principal elements in near-equiatomic proportions[1, 2] that tend to form simple solid solutions during solidification, instead of inter-metallic compounds, owing to high mixing entropy[3]. HEAs have been identified as promising candidates for various heterogeneous catalysis and electrocatalysis applications[4-9]. For instance, Qiu et al. developed a nanoporous AlNiCuPtPdAu materials for the oxygen reduction reaction (ORR). The resulting catalyst exhibited greatly enhanced high temperature stability and displayed redox activity up to ten times higher than the characteristics of Pt/C catalysts[10]. For the CO_2 reduction reaction, superior durable catalytic hydrogenation of CO_2 was demonstrated using CoNiCuRuPd HEA nanoparticles[11]. HEAs have also received much attention in recent years due to their unique mechanical properties, such as high strength and strain hardening ability[12-15]. Additionally, HEAs have shown noteworthy chemical properties, including corrosion and oxidation resistance[16-18]. The peculiar behavior of HEA in various applications, is primarily attributed to four core effects[3, 19-21].

- The high entropy effect impedes segregated phase formation. Mixing five or more elements increases the configurational entropy of HEA solid solution sufficiently to have a dominant effect on phase Gibb's energy stabilizing a solid solution instead of intermetallic phases.

- Lattice distortion effects alter the crystalline structure. In HEAs, each atom is surrounded by atoms of different elements, causing significant lattice distortion due to atomic size differences and varying bonding energies. This distortion can affect the mechanical, thermal, electrical, optical, and chemical properties of HEAs.

- Sluggish diffusion hampers phase transformation. The presence of multiple elements creates fluctuations in lattice potential energy, leading to low-energy sites that trap atoms and hinder diffusion. This results in slower grain growth, increased recrystallization temperature, enhanced creep resistance[22-25].

- Cocktail effects lead to properties that are different from those predicted by the mixture rule. It refers to the surprising and exotic properties that can arise in HEAs due to their complex compositions. Described as the "overall effect resulting from mutual interactions among composing elements"[26] this effect is not exclusive to HEAs and is often considered as an abstract effect emerging from the previous effects.

Those four core effects are more pronounced in HEAs than in other classical alloys and strongly influence their properties and behavior. The crux of these 4 effects lies in the concept of

"mixing". The homogeneity of the alloy is normally assessed using panels of physico-chemical characterization tools. X-Ray Diffraction (XRD) provides insights into the crystallographic structure. X-Ray Photoelectron Spectroscopy (XPS) analyzes the chemical environment including elemental composition and oxidation states on the surface and subsurface regions. Electron microscopy (TEM, SEM, STEM) is often coupled with local elemental analysis (EDX) to reveal local information such as the element distribution[27]. Often, a link can be made between the quality of the mixing in the alloy and the emergence of peculiar properties or performance[28-30]. However, the most classical characterization techniques mentioned above, approach the concept of homogeneity either indirectly (e.g. observing lattice distortion) or with a limited spatial resolution or limited sensitivity (e.g. elemental mapping by STEM-EDX). We argue that, beyond this rough description of "homogeneity", the parameter that truly determines the properties of the alloys is the "atomic level degree of mixing". Thus, it becomes essential to verify and quantify the alloying of the different elements at the atomic scale.

ToF-SIMS provides detailed chemical information about the top atomic layers of a sample[31]. The technique involves bombarding the sample surface with a pulsed primary ion beam under ultra-high vacuum conditions[32], generating secondary ions that carry chemical information about the surface and that can be separated based on their masses. ToF-SIMS was proven powerful for the characterization of heterogeneous catalysts, e.g. to probe the dispersion of active elements[33], to assess the interaction between different components[34], or to study the cause of deactivation[35]. ToF-SIMS has already been used to analyze sample composition in narrow trenches of 20 nm in width[36, 37]. Additionally, ToF-SIMS has been utilized to gather information about the correlated presence of two metals in mixed oxide nanoparticles with sizes down to a few nanometers[38, 39]. In these studies, sputtered cluster ions are used to assess the intimate mix of their elemental constituents in the solid. The rationale is that the craters formed by energetic cluster ions, such as 30 keV Bi_{3-5}^+, in inorganic solid must be formed within a single impact event. Thus, their constituents must arise from the same nanovolume area. Molecular dynamics simulations confirmed that clusters containing more than 2-3 atoms are often emitted as such (i.e. without recombination above the surface), implying that they were direct neighbors in the solid[40].

Here, we show that ToF-SIMS can be used to demonstrate that alloying exists at the atomic scale in HEAs and to quantitatively assess the atomic level degree of mixing at their surface. We exploit the identification and quantification of these secondary ions to gain insights on the intimacy of the metal mixing and on the presence of oxidized species at the alloy surface. We demonstrate that increasing composition complexity (and therefore the entropy) leads to (i) more homogeneous atomic mixing at the atomic scale and (ii) higher resistance against surface oxidation (i.e. passivation). To test these hypotheses, two models porous HEAs (41) based on Ru, Pt, Pd, Ir, and Rh are used as the case study. One well mixed at the atomic scale level (denoted "HEA Mix") and another showing phase segregation (denoted "HEA Seg"). A series of less complex alloys based on the same metals were also analyzed as benchmarks: pure Ru, binary Ru-Pt, Ru-Pd, Ru-Ir and Ru-Rh alloys, ternary Ru-Pt-Pd alloy, and quaternary Ru-Pt-Pd-Ir alloy (Table S1).

EXPERIMENTAL

Synthesis of the Porous Alloys. Samples were synthetized using the protocol designed by de Marco et al.[41]. A detailed protocol can be found in Electronic Supporting information (ESI).

ToF-SIMS Spectra Acquisition. The acquisition of ToF-SIMS data was carried out using an IONTOF ToF-SIMS[5] instrument (installed in 2010 from Münster, Germany). A Liquid Metal Ion Gun (LMIG) source of Bi_n^+ (n = 1, 3, 5) and Bi_3^{++} in high current bunch mode was employed, with a pulsed current ranging between 0.05 and 1 pA. To prevent surface charging caused by the charge of the sample holder, a flood gun of 20 eV was employed. The actual data acquisition was performed over a surface area of 150µm × 150µm and the ion dose for the Bi_5^+ values are displayed in the Table S2. The operation was carried out using a cycle time of 150 µs resulting of an 0-1800 m/z mass range. The analysis time was of 2 minutes for each sample and a charge compensator was used to avoid charges accumulation on the sample surface. These parameters were specifically selected to optimize the detection of clusters of high mass.

For each sample, the acquisition was performed in five separate repetitions for each primary ions species to provide substantial data for subsequent statistical analyses. Analyses were carried out in both positive and negative ion modes. Throughout the acquisition process, there is a shift in the spectrum peaks, necessitating calibration. This calibration was carried out using CH_3^+, $C_2H_5^+$, $C_3H_5^+$, and $C_4H_7^+$ peaks in positive mode, and CH^-, C_2H^-, C_3H^-, and C_4H^- peaks in negative mode. An automatic identification and quantification of the pattern of peaks was applied on all spectra, after a binning and a normalization (as discussed in the following section). For a detailed description of analysis conditions, binning, and normalization steps, the reader is referred to the ESI.

Automatic Cluster Peak Identification and Quantitative Processing. In ToF-SIMS, each chemical species produces a unique peaks pattern following its specific isotopic distribution. Some elements, such as Rh, exhibit simple distributions with a single peak at 103 m/z. In contrast, elements such as Ru and Pd generate broader peaks patterns due to the presence of multiple isotopes. When analyzing a sample containing Ru, Pd, and Rh, the resulting peaks pattern, known as the composite mass spectrum, is a combination of the individual isotopic distributions of these three elements as illustrated in Figure 1. This phenomenon becomes significantly complex when considering polyatomic species such as Ru_2, Ru_3, or mixed-element species such as RuPd, Ru_2Pd, Ru_2Pd_2, RuPdPd, and $RuPd_2Pd_2$. The composite mass spectra obtained at these m/z values represent a combination of the isotopic distribution and of all the polyatomic species of the different atoms. Decomposing these composite mass spectra into the individual isotopic mass distributions of each poly atomic chemical species is challenging and nearly impossible to accomplish manually due to the intricate overlap and the sheer number of possible cluster combinations. This complexity necessitates computational methods to separate and quantify the contributions of the isotopic distributions of each chemical species into the composite mass spectrum observed. The method that was designed to process quantitatively the ToF-SIMS data set is explained in detail in ESI. Essentially, it is based on the resolution of a matrix system that leads to a vector $\tilde{\boldsymbol{x}}$ containing the calculated abundances of each species.

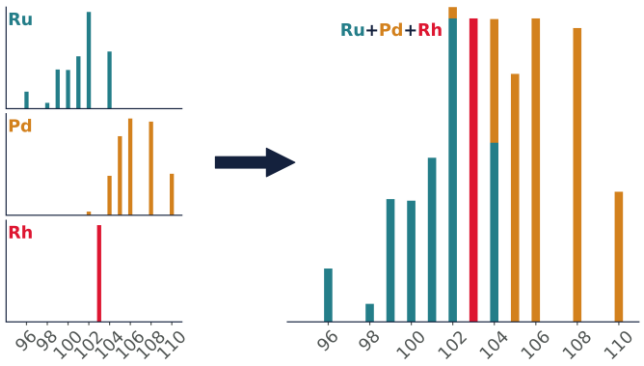

Figure 1: Schematic illustration of the overlapping isotopic distributions of Ru, Pd, and Rh. The peaks pattern (left column) merge to form a composite mass spectrum (right column), representing the cumulative isotopic distribution of the three elements.

RESULTS AND DISCUSSION

Sample Description: Morphology, Texture, Structure. A set of porous alloys was prepared by the method of De Marco et al.[41] (see Table S1). The key steps of the synthesis are summarized as follows: metal chloride precursors are mixed with PMMA beads. The resulting solution is then spray dried and annealed under Ar. During annealing, the polymer serves both as a pore-generating and as a reducing agent, leading to porous spherical metallic particles. One HEA containing five elements was synthesized, comprising Ru, Pt, Pd, Ir, and Rh in equal mass proportions of 20 wt.%. This sample is denoted "HEA Mix". In addition, a series of less complex samples was prepared: one pure Ru, four binary, one ternary and one quaternary alloys. The binary alloys were composed of 80 wt.% Ru and 20 wt.% of a second metal: Pt, Pd, Ir, or Rh. The ternary alloy was created with a mass ratio of 60 wt.% Ru, 20 wt.% Pt, and 20 wt.% Pd. The quaternary alloy was formulated with Ru, Pt, Pd, and Ir in a mass ratio of 40-20-20-20. For all these alloys, only the composition was varied, all other parameters (the proportion of PMMA, spraying and annealing parameters) were kept constant. HEA Mix was reported to show good mixing, having showed no sign of phase segregation in Scanning Electron Microscopy with Energy Dispersive X-Ray Analysis (SEM-EDX) as abundantly discussed by De Marco *et al.*[41]. Finally, one HEA with the same composition as HEA Mix was synthetized using the same protocol, except that no PMMA was introduced and a 10% H_2 was add to the Ar flux during the annealing process. This sample is denoted as "HEA Seg", as phase segregation was found in this case, as clearly evidenced by SEM EDX (Figure S1 and S2).

The main features of HEA Mix can be summarized as follows: it consists of macroporous nanoparticles with a size ranging from 0.5 to 5 µm and pore diameters of approximately 200 nm (Figure 2). The wall of these macropores are themselves mesoporous (5.4 nm and smaller) resulting in a specific surface area of about 100 m^2/g.

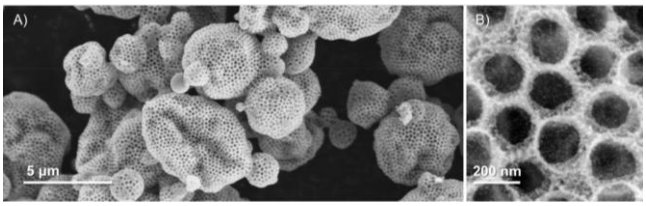

Figure 2: Scanning Electron Microscopy (SEM) images of the resulting macroporous nanoparticles at the particles scale (A), and at the pores scale (B) (reproduced from De Marco et al.[41] with permission from ACS).

X-ray diffractograms (Figure S3) obtained from the pure Ru sample show the typical hexagonal close-packed (HCP) structure characteristic of metallic Ru (PDF 06-0663), with the main diffraction lines at $2\theta \cong 44°$. Applying the Scherrer equation[42] of the 44° peak reveals an average crystallite size of about 7 nm. For binary alloys, the introduction of Pt to Ru did not significantly alter the broadness of the peaks. However, when Pd was added to the alloy, the XRD diffractogram demonstrated noticeably narrower peaks. The peak narrowing was more evident upon the addition of either Rh or Ir. These narrower peaks suggest a larger mean crystallite size. Applying the Scherrer equation, the mean crystallite size for Ru-Pt, Ru-Pd, Ru-Rh and Ru-Ir samples are respectively 8, 10, 24 and 29 nm.

When examining the ternary, quaternary, and quinary alloys, the situation is slightly different. The ternary alloy appears to exhibit broader peaks on the XRD diffractogram, suggesting smaller crystallites. However, the coexistence of two phases within the material complicates the interpretation. The diffractogram for the quaternary alloy demonstrates wider peaks, indicating smaller crystallites (~6 nm) compared to the binary alloys. The trend of decreasing crystallite size persists in the quinary alloy (HEA Mix), which exhibits the broadest peaks, corresponding to a mean crystallite size of about 5 nm.

Further comparison of the samples diffractogram with the theoretical metallic phases also reveals some interesting facts. The Ru HCP phase is maintained in the binary alloys (Ru-Pt, Ru-Pd, Ru-Rh and Ru-Ir). Yet, in the ternary alloys (Ru-Pt-Pd), an additional face-centered cubic (FCC) phases also appears, growing more intense as we move from the ternary to the quaternary alloy (Ru-Pt-Pd-Ir), at the expense of the HCP phase. In HEA mix and HEA Seg, only the FCC phase is detected.

Since the theoretical FCC phases of all five elements are quite similar, it is not possible to assess solely based on the XRD whether the HEA is well mixed at an atomic level. Indeed, the seemingly single FCC phase in the HEA could either result from a single phase containing all five elements or from the HEA being constituted of small pure FCC crystallites, each made of one single element. This ambiguity explains why the diffractograms of the HEA Seg and Mix are similar. It constitutes a rationale for using ToF-SIMS, as a technique capable of providing an elemental footprint of the atomic-level mixing.

Optimization of the ToF-SIMS Analysis. In ToF-SIMS, the nature of the primary ion affects the yield and fragmentation of secondary ions[43]. The kinetic energy (E_k) of the primary ions used in ToF-SIMS is described by (Eq. *1*)

$$E_k = qV \qquad \text{(Eq. 1)}$$

where q is the charge and V is the voltage. This implies that the kinetic energy depends only on the particle's charge, not on its mass. Consequently, primary particles with a given charge

have a specific kinetic energy. However, the distribution of this energy among the atoms in the primary particle varies with the number of atoms. For instance, a Bi_1^+ ion and a Bi_5^+ ion both have the same total kinetic energy, but the energy per atom in Bi_5^+ is one-fifth that of Bi_1^+. This variation of the energy per atom (depending on the nature of primary ion) influences the ion penetration in the solid and the sputtering process, including the secondary ion yields and fragmentation patterns observed in ToF-SIMS[40, 44]. To best quantify the atomic degree of mixing of the samples, the high mass secondary clusters are the most important since they can be taken as the markers of a well atomically mixed alloy. Similarly, for the examination of the oxidation resistance of the samples, the secondary clusters of interest are oxides. To determine which primary ion would provide the highest yield for the secondary clusters of interest, a Principal Component Analysis (PCA) was applied on a series of acquisitions made on the Ru-Pt-Pd-Ir alloy analyzed with 4 different primary ions (Bi_1^+, Bi_3^+, Bi_3^{++} and Bi_5^+). Upon the analysis of the Scores and Loadings plots (See Figure S8 and S9), Bi_5^+ was identified as the best primary ion to measure high yields of large clusters and oxides. Therefore, the following results will only use data from the analysis performed with Bi_5^+.

Peak Identification and Quantitative Analysis. As a case study, we here describe the quantitative processing of the data obtained looking exclusively for the isotopic distributions of Ru, Pd and Rh in the HEA Mix sample analyzing the HEA Mix sample. Figure 3A compares the observed spectrum ($\tilde{\boldsymbol{Y}}_{\boldsymbol{obs}}$) with the computed spectrum ($\tilde{\boldsymbol{Y}}_{\boldsymbol{calc}}$) for the m/z range of 95 to 111, showing close alignment for most m/z values. Small discrepancies between the observed and calculated spectra are visible at m/z values of 97, 107 and 109. This suggests either the presence of other elements/molecules not considered in the model, or simply noise associated with the measurement itself.

Using the data processing framework outlined above, it is possible to visualize a detailed breakdown of the isotopic contributions from Ru, Rh, and Pd (Figure 3B). The teal bars represent the isotopic distribution of Ru, with the most intense peaks at m/z values 96, 98, 100, 101, 102, and 104, and a calculated abundance of $\tilde{\boldsymbol{x}}_{\boldsymbol{Ru}} = 6325$. The red bars indicate the distribution of Rh, with a prominent peak at 103 m/z, which matches the observed spectra closely, confirming the presence of Rh with a calculated abundance of $\tilde{\boldsymbol{x}}_{\boldsymbol{Rh}} = 3665$. The orange bars depict the distribution of Pd, showing contributions at m/z values 102, 104, 105, 106, 108, and 110, with a calculated abundance of $\tilde{\boldsymbol{x}}_{\boldsymbol{Pd}} = 5808$. This example validates our process for identification and quantification in this range of m/z values.

However, at higher m/z values, the lower signal-to-noise ratio leads to a decrease of the quality of the fit, as illustrated in Figure 4. In the 650 to 1550 m/z range, the overall alignment between observed and computed spectra (Figure 4A) suggests the model is capturing the major peaks, but discrepancies are noticeable in certain regions. The breakdown of individual isotopic contributions (Figure 4B) is significantly more complicated, with many overlapping distributions, which makes asserting the fit quality difficult. A similar quality of fit is observed for an intermediate m/z range of 150 to 650 (Figure S6). Despite the imperfection of the fit, it has been chosen to use the values of the calculated abundances ($\tilde{\boldsymbol{x}}$) along all m/z values for all the analyses in the following sections of this paper. The lower precision of calculated abundances at high m/z values was verified to have a negligible impact on the final results, due to the low intensity of these signals, as compared to the intensity at lower m/z. For the subsequent analyses, all adducts (e.g. Bi adducts, Figure S7) were excluded.

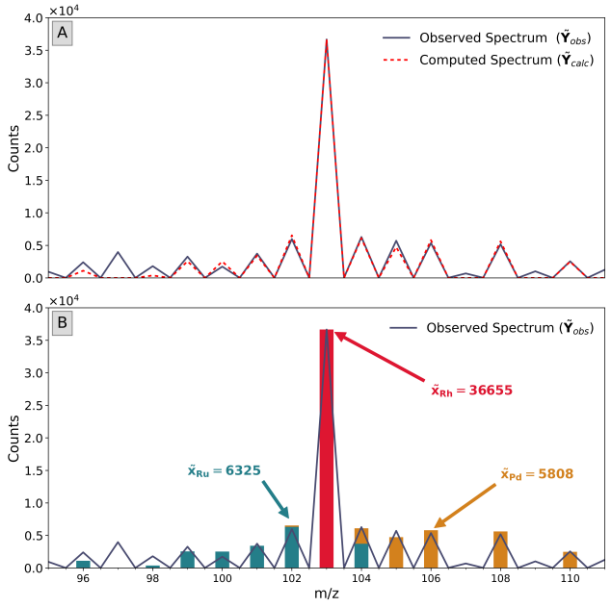

Figure 3: Comparison of observed and computed spectra for the m/z range 95 to 111 for the HEA Mix. A: The observed spectrum ($\tilde{\boldsymbol{Y}}_{obs}$, solid blue line) closely aligns with the computed spectrum ($\tilde{\boldsymbol{Y}}_{calc}$, dashed red line). B: Detailed breakdown showing the individual isotopic contributions as well as their abundance ($\tilde{\boldsymbol{x}}$) of Ru (teal bars), Rh (red bars), and Pd (orange bars) within the composite mass spectrum.

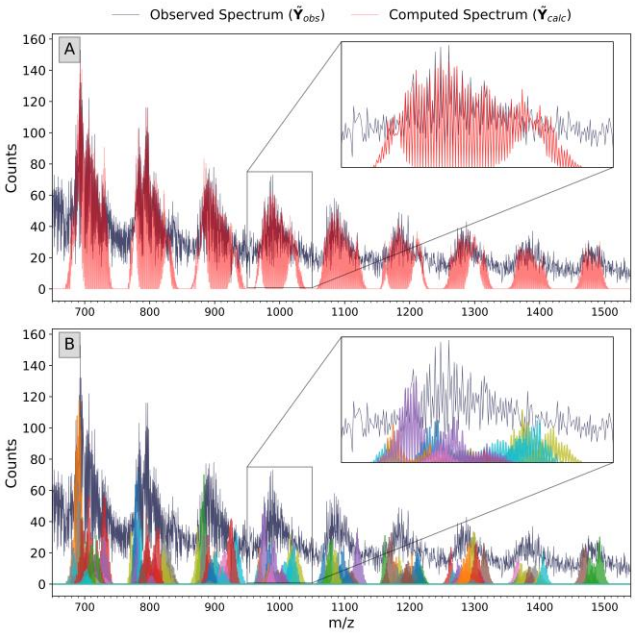

Figure 4: Comparison of observed ($\tilde{\boldsymbol{Y}}_{obs}$) and computed spectra ($\tilde{\boldsymbol{Y}}_{calc}$) for the m/z range of 650 to 1550 for the HEA Mix. A: plot of the overall alignment of the spectra, with an inset highlighting a detailed region. B: display of the individual isotopic contributions (each color representing different isotopic species).

Assessment of the atomic-level degree of mixing. The main challenge in ToF-SIMS quantification is the variation of yields for a given ion across different samples solely due to the

chemical environment of each sample (i.e. the "matrix effect"). For instance, Figure S10 shows that the normalized count for Ru^+ – which is the count of Ru^+ ions detected divided by the total count of all detected ions – varies across the four binary alloys, despite their identical loading of Ru in their mass composition (80 wt.%). The normalized count for Ru is particularly high for Ru-Pt and particularly low for Ru-Pd. The difference in Ru counts is mainly due to such matrix effects. This calls for further data treatment for the dataset to be exploitable.

To address this issue, we developed an indicator called the Cluster Ratio (CR). CR is defined as the ratio between all the Hetero Atomic Clusters (i.e., clusters that contain at least two different atoms such as RuPt, RuPtPd, etc.) and all the Homo Atomic Clusters (i.e., clusters that contain only one type of atom such as Ru_2, Ru_3, etc.). Thus, the CR is expressed by (Eq. 2).

$$CR = \frac{HeACS}{HoACS} \quad \text{(Eq. 2)}$$

With HeACS and HoACS being the Hetero and Homo Atomic Cluster Sums. Those Sums are defined respectively as the sums of Hetero and Iso Atomic Clusters (Eq. 3) and (Eq. 4).

$$HeACS = \sum_a \sum_b \sum_c \sum_d \sum_e [Ru_a Pt_b Pd_c Ir_d Rh_e^+] \quad \text{(Eq. 3)}$$
$$\forall a,b,c,d,e = 0,1,2,3,4,5$$
$$with\ at\ least\ 2\ of\ \{a,b,c,d,e\}\ are\ non\ zero$$

$$HoACS = \sum_a [Ru_a^+ + Pt_a^+ + Pd_a^+ + Ir_a^+ + Rh_a^+] \quad \text{(Eq. 4)}$$
$$\forall a = 2,3,4,5$$

Thus, this ratio represents the prevalence of Hetero Atomic clusters in relation to Homo Atomic Clusters. A higher CR implies a better mixing at the level of the atoms in the sample, providing a more reliable assessment of the atomic-level degree of mixing. The CR can mitigate the problem of varying secondary ion yields across samples because it is hypothesized that the matrix effect for the HeACR is the same for the HoACR. By taking the ratio of these two values, the influence of the matrix effect is effectively normalized, leading to a more accurate comparison of atomic-level mixing across different samples.

From the sample series analyzed in this study, a discernible pattern is observed with the CR generally increasing along with the number of components in the alloy (Figure 5 (top)). For the pure Ru sample, the CR is obviously zero, since no hetero atomic clusters are present. The binary alloys (Ru-Pt, Ru-Pd, Ru-Ir, and Ru-Rh) show varying CR values, reflecting the influence of the second element on the mixing. Notably, Ru-Pt has a higher CR compared to Ru-Pd, indicating better atomic mixing in the Ru-Pt alloy. As we progress to ternary and quaternary alloys (Ru-Pt-Pd and Ru-Pt-Pd-Ir), there is a noticeable increase in the CR, suggesting improved atomic-level degree of mixing with the addition of more elements. The highest CR values are observed in the HEA samples, demonstrating that HEAs exhibit the most significant degree of atomic-level mixing among the samples analyzed. Overall, a clear trend of increasing CR with the number of elements in the alloy is illustrated, highlighting superior atomic mixing when compositional complexity increases, with a culmination in high entropy alloy sample. It is notable this trend is respected also for the ternary and quaternary alloys, despite the observation of two crystalline phase in the XRD results (FCC and HCP) within the ternary and quaternary alloys. Importantly, HEA Mix scores higher than HEA Seg in terms of CR, supporting the observations made with other characterization technique (SEM-EDX, see ESI), hinting at phase segregation in HEA Seg. This observation further validates the proposed quantitative processing approach.

The significance of the differences in CR values has been statistically assessed by pairwise t-tests and the results are available in Sections S5.1, S5.2 and S5.3 of the ESI. CR values are not statistically different among the various binary alloys. However, CR values calculated for ternary, quaternary, HEA Mix, and HEA Seg samples are significantly higher, confirming the trend that atomic mixing improves with compositional complexity.

One of the main challenges with the CR metric as currently defined is the fact that it includes Ru, whose loading varies across the samples, possibly skewing the results. To address this, an "adjusted" CR can be calculated, to focus on different subset of metals, excluding Ru in the HeACS and HoACS sums. Such adjusted CR allow for example to interrogate the degree of mixing between Pt and Pd in the series of alloys which have the same Pd and Pt loading but different compositional complexity (Ru-Pt-Pd, Ru-Pt-Pd-Ir and the two HEA samples). The results and statistical significance of these adjusted CRs are detailed in the Section S5.4 of the ESI. A consistent trend is observed, showing an increase in CR value with the number of components, which mirrors the trend observed with the original CR. The statistical significance of these trends, indicates that while the directionality of the trends is consistent, the differences between sample are less significant compared to the original CR differences. In summary, whether we look at the entire composition of the alloys or just at subsets of metals, CR metrics consistently reinforce the central thesis of this study that compositional complexity enhances atomic mixing.

Oxidation resistance. As mentioned earlier, HEAs often display superior oxidation resistance compared to conventional alloys. In an attempt to quantify this trait using ToF-SIMS data, a new metric, the Oxide Ratio (OR), was formulated. The negative polarity was used in this case, because the yield for oxidic species is much higher than in the positive mode. Thus, OR is here defined as the ratio of the sum of all oxide ions (MO_x^-) present in the sample to the sum of M^- species present in the sample. For example, for the HEA alloys (Ru-Pt-Pd-Ir-Rh), the OR is expressed by (Eq. *5*).

$$OR = \sum_x \left[\frac{RuO_x^- + PtO_x^+ + PdO_x^- + IrO_x^- + RhO_x^-}{Ru^- + Pt^- + Pd^- + Ir^- + Rh^-}\right] \quad \text{(Eq. 5)}$$
$$\forall x = 1,2,\ldots$$

This ratio represents the propensity of the metal components of the alloy to undergo surface passivation, i.e. to form oxide species. Furthermore, by individually examining each component in the numerator, it becomes possible to discern which metallic component is most susceptible to oxidation and how varying chemical conditions may influence this propensity.

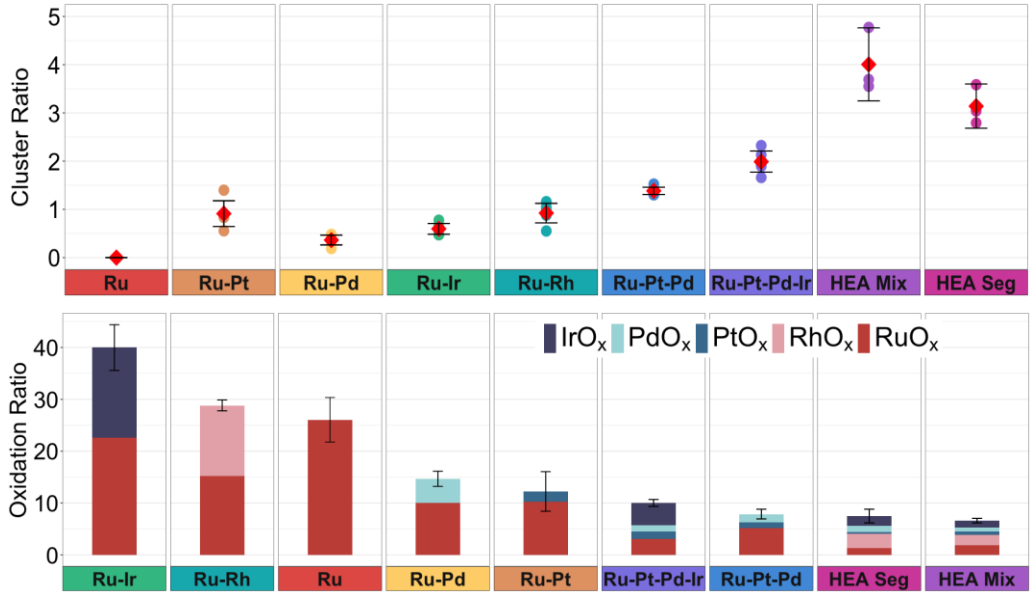

Figure 5: (top) Value (colored point), mean value (red diamonds) and 95% confidence intervals (black error bars) of the Cluster Ratio across the nine samples in positive mode with Bi_5^+. (bottom) Mean composition of the Oxide Ratio across all the samples in Bi_5^+ in negative mode. The 95% confidence intervals are represented with the black error bars

The OR was calculated for all the samples, considering all metals (Figure 5 (bottom)) and Section S6.1 in the ESI for a discussion on the statistical significance of the trends discussed here). From this analysis, it emerged that OR markedly decreased when the number of elements in the alloy increases (with the exception of Ru vs Ru-Ir and Ru-Rh). This hints towards a correlation between oxidation resistance and the number of components in the alloy. In particular, HEA Mix showed the lowest OR value, confirming – at the atomic level – a property that is well documented[45-47]. Additionally, the HEA Seg sample exhibited a higher OR compared to the HEA Mix, suggesting a positive effect of the atomic-level degree of mixing on oxidation resistance.

To understand this trend, it is essential to consider the oxophilicity of the metals involved, i.e. their tendency to form oxides. The oxophilicity values for Ru, Ir, and Rh are 0.4, 0.4, and 0.3, respectively, which are significantly higher than those for Pt (0.1) and Pd (0.0)[48]. This greater propensity to form oxides may be contributing to the elevated levels of OR observed for the Ru-Ir, Ru, and Ru-Rh samples compared to Ru-Pd and Ru-Pt ones. Thus, the decrease in OR when increasing compositional might simply be related to the fact that the Ru content decreases when adding other metals (from 100% to 20% as sample complexity increases). Since Ru is the most oxophilic metal in the series, it is no surprise that the overall OR decreases with the diminution of Ru. To mitigate the impact of the differences in Ru loadings across the samples set, the individual OR of each different metal (except Ru) were examined. The Oxidation Ratio of a given metal M is defined by (Eq. *6*)

$$R_M = \sum_x \left[\frac{MO_x^-}{M^-}\right] \quad \forall x = 1,2,\ldots \qquad \text{(Eq. 6)}$$

This analysis revealed the same decreasing trend (Figure 6). The binary alloys consistently showed the highest OR values, and this value decreased when compositional complexity increases, with HEA Mix showing the lowest OR values. One exception to this trend was found for Pt (Ru-Pt-Pd-Ir alloy has a higher OR value than the Ru-Pt-Pd alloy, and HEA Mix shows a higher OR value than HEA Seg). This could indicate an abnormal effect of the atomic-level degree of mixing on Pt oxide formation. Statistical assessments were conducted using pairwise t-tests (see Section S6.2); the differences were statistically significant.

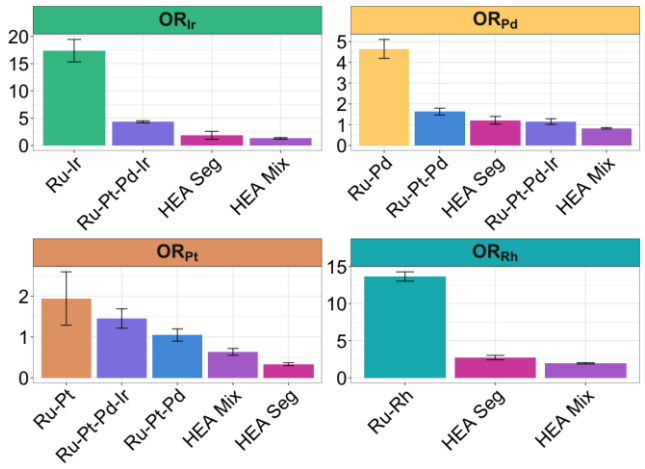

Figure 6: Mean value of individual metal Oxidation Ratio in Bi5+ in negative mode. The 95% confidence intervals are represented with the black error bars.

CONCLUSION AND OUTLOOK

In this work, ToF-SIMS has been used to gain a deeper understanding of the surface of High Entropy Alloys at the atomic scale. To handle the complexity of ToF-SIMS spectra resulting from HEAs, an automatic identification and quantitative

processing framework was developed, allowing to manage the large group of peaks and ensuring accurate decomposition of isotopic mass distributions from the composite mass spectrum. From this analysis, the contribution of each cluster could be exploited to shed light on the properties of the alloys surface.

We introduced two key metrics: the Cluster Ratio and the Oxide Ratio. The Cluster Ratio effectively quantified the degree of atomic-level mixing across various HEA samples. We observed a clear trend of increasing CR with the number of alloyed elements, indicating improved atomic mixing in more complex alloys. The HEA Mix sample, showing no phase segregation, exhibited the highest CR, validating its superior atomic homogeneity compared to the HEA Seg sample, which displayed elemental segregation. The Oxide Ratio unambiguously confirmed, in a quantitative way, that increasing elemental complexity enhances resistance to surface oxidation. The HEA Mix sample demonstrated the lowest OR, consistent with its higher degree of atomic mixing. This corroborates the known superior oxidation resistance of HEAs.

Overall, this work illustrates that ToF-SIMS is a highly useful technique for analyzing complex materials such as HEAs, offering detailed chemical information about the top layers of a sample and enabling the assessment of atomic-level degree of mixing and surface passivation.

ASSOCIATED CONTENT

Supporting information. The electronic supporting information is available free of charges at (ACS URL) include supplemental characterization, synthesis methods, ToF-SIMS spectra numerical methods as well as statistical assessment.

Data availability. Code scripts for data extraction, treatment, statistical tests, plot generation, raw and processed XRD diffractograms and ToF-SIMS spectra, are available in a comprehensive repository on GitHub accessible via this link: https://github.com/Oscar-Laurent/ToF-SIMS_Article.

AUTHOR INFORMATION

Corresponding authors

Arnaud Delcorte and **Damien P. Debecker** - Institute of Condensed Matter and Nanosciences (IMCN), Université catholique de Louvain (UCLouvain), Louvain-la-Neuve, 1348, Belgium arnaud.delcorte@uclouvain.be and damien.debecker@uclouvain.be

Authors

Oscar F. Laurent, Claude Poleunis - Institute of Condensed Matter and Nanosciences (IMCN), Université catholique de Louvain (UCLouvain), Louvain-la-Neuve, 1348, Belgium
Maria Letizia De Marco, Marco Faustini, Cédric Boissière - Laboratoire Chimie de la Matiere Condensée de Paris (LCMCP), Sorbonne Université–CNRS, 4, Place Jussieu, 75005 Paris, France

Authors Contribution

The Manuscript was written through contribution of all authors; they have given approval to the final version of the manuscript.

Notes

The authors declare no competing financial interests

ACKNOWLEDGEMENT

OL thanks the Fonds Spécial de la Recherche of UCLouvain for granting a PhD fellowship in the framework of the "HEAT" project. DPD thanks the Francqui Foundation for the Francqui Research Professor chair. AD is a research director of FNRS. MDM and MF acknowledge funding from the European Research Council (ERC) under European Union's Horizon 2020 Programme (Grant Agreement no. 803220, TEMPORE).

REFERENCES

1. Yeh, J. W.; Chen, S. K.; Lin, S. J.; Gan, J. Y.; Chin, T. S.; Shun, T. T.; Tsau, C. H.; Chang, S. Y., Nanostructured high-entropy alloys with multiple principal elements: novel alloy design concepts and outcomes. *Advanced engineering materials* **2004,** *6* (5), 299-303.
2. Cantor, B.; Chang, I. T. H.; Knight, P.; Vincent, A. J. B., Microstructural development in equiatomic multicomponent alloys. *Materials Science and Engineering: A* **2004,** *375*, 213-218.
3. George, E. P.; Raabe, D.; Ritchie, R. O., High-entropy alloys. *Nature reviews materials* **2019,** *4* (8), 515-534.
4. Xin, Y.; Li, S.; Qian, Y.; Zhu, W.; Yuan, H.; Jiang, P.; Guo, R.; Wang, L., High-entropy alloys as a platform for catalysis: progress, challenges, and opportunities. *Acs Catalysis* **2020,** *10* (19), 11280-11306.
5. Furukawa, S.; Komatsu, T.; Shimizu, K.-i., Catalyst design concept based on a variety of alloy materials: a personal account and relevant studies. *Journal of Materials Chemistry A* **2020,** *8* (31), 15620-15645.
6. Wu, D.; Kusada, K.; Yamamoto, T.; Toriyama, T.; Matsumura, S.; Gueye, I.; Seo, O.; Kim, J.; Hiroi, S.; Sakata, O.; others, On the electronic structure and hydrogen evolution reaction activity of platinum group metal-based high-entropy-alloy nanoparticles. *Chemical science* **2020,** *11* (47), 12731-12736.
7. Yao, Y.; Liu, Z.; Xie, P.; Huang, Z.; Li, T.; Morris, D.; Finfrock, Z.; Zhou, J.; Jiao, M.; Gao, J.; others, Computationally aided, entropy-driven synthesis of highly efficient and durable multi-elemental alloy catalysts. *Science Advances* **2020,** *6* (11), eaaz0510.
8. Li, H.; Han, Y.; Zhao, H.; Qi, W.; Zhang, D.; Yu, Y.; Cai, W.; Li, S.; Lai, J.; Huang, B.; others, Fast site-to-site electron transfer of high-entropy alloy nanocatalyst driving redox electrocatalysis. *Nature communications* **2020,** *11* (1), 5437.
9. Bridges, D.; Fieser, D.; Santiago, J. J.; Hu, A., Novel Frontiers in High-Entropy Alloys. *Metals* **2023,** *13* (7), 1193.
10. Qiu, H.-J.; Fang, G.; Wen, Y.; Liu, P.; Xie, G.; Liu, X.; Sun, S., Nanoporous high-entropy alloys for highly stable and efficient catalysts. *Journal of Materials Chemistry A* **2019,** *7* (11), 6499-6506.
11. Mori, K.; Hashimoto, N.; Kamiuchi, N.; Yoshida, H.; Kobayashi, H.; Yamashita, H., Hydrogen spillover-driven synthesis of high-entropy alloy nanoparticles as a robust catalyst for CO2 hydrogenation. *Nature communications* **2021,** *12* (1), 3884.
12. Zhu, J. M.; Fu, H. M.; Zhang, H. F.; Wang, A. M.; Li, H.; Hu, Z. Q., Synthesis and properties of multiprincipal component AlCoCrFeNiSix alloys. *Materials Science and Engineering: A* **2010,** *527* (27-28), 7210-7214.
13. Zhou, Y. J.; Zhang, Y.; Wang, Y. L.; Chen, G. L., Solid solution alloys of Al Co Cr Fe Ni Ti x with excellent room-temperature mechanical properties. *Applied physics letters* **2007,** *90* (18), 181904.
14. Chen, S.-T.; Tang, W.-Y.; Kuo, Y.-F.; Chen, S.-Y.; Tsau, C.-H.; Shun, T.-T.; Yeh, J.-W., Microstructure and properties of age-hardenable AlxCrFe1. 5MnNi0. 5 alloys. *Materials Science and Engineering: A* **2010,** *527* (21-22), 5818-5825.
15. Tong, C.-J.; Chen, M.-R.; Yeh, J.-W.; Lin, S.-J.; Chen, S.-K.; Shun, T.-T.; Chang, S.-Y., Mechanical performance of the Al x CoCrCuFeNi high-entropy alloy system with multiprincipal elements. *Metallurgical and Materials Transactions A* **2005,** *36*, 1263-1271.
16. Lin, C.-M.; Tsai, H.-L., Evolution of microstructure, hardness, and corrosion properties of high-entropy Al0. 5CoCrFeNi alloy. *Intermetallics* **2011,** *19* (3), 288-294.
17. Chen, Y. Y.; Duval, T.; Hong, U. T.; Yeh, J. W.; Shih, H. C.; Wang, L. H.; Oung, J. C., Corrosion properties of a novel bulk Cu0. 5NiAlCoCrFeSi glassy alloy in 288° C high-purity water. *Materials Letters* **2007,** *61* (13), 2692-2696.

18. Chou, Y. L.; Wang, Y. C.; Yeh, J. W.; Shih, H. C., Pitting corrosion of the high-entropy alloy Co1. 5CrFeNi1. 5Ti0. 5Mo0. 1 in chloride-containing sulphate solutions. *Corrosion Science* **2010,** *52* (10), 3481-3491.
19. He, B.; Zu, Y.; Mei, Y., Design of advanced electrocatalysts for the high-entropy alloys: Principle, progress, and perspective. *Journal of Alloys and Compounds* **2023,** *958*, 170479.
20. Tsai, M.-H., Physical properties of high entropy alloys. *Entropy* **2013,** *15* (12), 5338-5345.
21. Miracle, D. B.; Senkov, O. N., A critical review of high entropy alloys and related concepts. *Acta Materialia* **2017,** *122*, 448-511.
22. Tong, C.-J.; Chen, Y.-L.; Yeh, J.-W.; Lin, S.-J.; Chen, S.-K.; Shun, T.-T.; Tsau, C.-H.; Chang, S.-Y., Microstructure characterization of Alx CoCrCuFeNi high-entropy alloy system with multiprincipal elements. *Metallurgical and Materials Transactions A* **2005,** *36* (4), 881-893.
23. Tsai, C.-W.; Chen, Y.-L.; Tsai, M.-H.; Yeh, J.-W.; Shun, T.-T.; Chen, S.-K., Deformation and annealing behaviors of high-entropy alloy Al0.5CoCrCuFeNi. *Journal of Alloys and Compounds* **2009,** *486* (1), 427-435.
24. Hsu, C.-Y.; Juan, C.-C.; Wang, W.-R.; Sheu, T.-S.; Yeh, J.-W.; Chen, S.-K., On the superior hot hardness and softening resistance of AlCoCrxFeMo0. 5Ni high-entropy alloys. *Materials Science and Engineering: A* **2011,** *528* (10-11), 3581-3588.
25. Senkov, O. N.; Wilks, G. B.; Scott, J. M.; Miracle, D. B., Mechanical properties of Nb25Mo25Ta25W25 and V20Nb20Mo20Ta20W20 refractory high entropy alloys. *Intermetallics* **2011,** *19* (5), 698-706.
26. Pickering, E. J.; Jones, N. G., High-entropy alloys: a critical assessment of their founding principles and future prospects. *International Materials Reviews* **2016,** *61* (3), 183-202.
27. Sun, Y.; Dai, S., High-entropy materials for catalysis: A new frontier. *Science Advances* **2021,** *7* (20), eabg1600.
28. Yao, Y.; Dong, Q.; Brozena, A.; Luo, J.; Miao, J.; Chi, M.; Wang, C.; Kevrekidis, I. G.; Ren, Z. J.; Greeley, J.; others, High-entropy nanoparticles: Synthesis-structure-property relationships and data-driven discovery. *Science* **2022,** *376* (6589), eabn3103.
29. Löffler, T.; Ludwig, A.; Rossmeisl, J.; Schuhmann, W., What Makes High-Entropy Alloys Exceptional Electrocatalysts? *Angewandte Chemie International Edition* **2021,** *60* (52), 26894-26903.
30. Moniri, S.; Yang, Y.; Ding, J.; Yuan, Y.; Zhou, J.; Yang, L.; Zhu, F.; Liao, Y.; Yao, Y.; Hu, L.; Ercius, P.; Miao, J., Three-dimensional atomic structure and local chemical order of medium- and high-entropy nanoalloys. *Nature* **2023,** *624* (7992), 564-569.
31. Vickerman, J. C., ToF-SIMS—an overview. *ToF-SIMS: surface analysis by mass spectrometry* **2001**, 1-40.
32. Benninghoven, A., The history of static SIMS-a personal perspective. *TOF-SIMS: materials analysis by mass spectrometry* **2013**.
33. Debecker, D. P.; Bouchmella, K.; Poleunis, C.; Eloy, P.; Bertrand, P.; Gaigneaux, E. M.; Mutin, P. H., Design of SiO ₂ −Al ₂ O ₃ −MoO ₃ Metathesis Catalysts by Nonhydrolytic Sol−Gel. *Chemistry of Materials* **2009,** *21* (13), 2817-2824.
34. Weng, L.-T., Advances in the surface characterization of heterogeneous catalysts using ToF-SIMS. *Applied Catalysis A: General* **2014,** *474*, 203-210.
35. Ruijten, D.; Narmon, T.; Van Aelst, K.; De Weer, H.; van der Zweep, R.; Hendrickx, T.; Poleunis, C.; Li, L.; Van Geem, K. M.; Debecker, D. P.; others, Tertiary Amines from RCF Lignin Mono-and Dimers: Catalytic N-Functionalized Antioxidants from Wood. *ACS Sustainable Chemistry & Engineering* **2023,** *11* (12), 4776-4788.
36. Spampinato, V.; Armini, S.; Franquet, A.; Conard, T.; Van Der Heide, P.; Vandervorst, W., Self-focusing SIMS: A metrology solution to area selective deposition. *Applied Surface Science* **2019,** *476*, 594-599.
37. Franquet, A.; Douhard, B.; Melkonyan, D.; Favia, P.; Conard, T.; Vandervorst, W., Self Focusing SIMS: Probing thin film composition in very confined volumes. *Applied Surface Science* **2016,** *365*, 143-152.
38. Ngnintedem Yonti, C.; Kenfack Tsobnang, P.; Lontio Fomekong, R.; Devred, F.; Mignolet, E.; Larondelle, Y.; Hermans, S.; Delcorte, A.; Lambi Ngolui, J., Green Synthesis of Iron-Doped Cobalt Oxide Nanoparticles from Palm Kernel Oil via Co-Precipitation and Structural Characterization. *Nanomaterials* **2021,** *11* (11), 2833.
39. Lontio Fomekong, R.; Kenfack Tsobnang, P.; Magnin, D.; Hermans, S.; Delcorte, A.; Lambi Ngolui, J., Coprecipitation of nickel zinc malonate: A facile and reproducible synthesis route for Ni1−Zn O nanoparticles and Ni1−Zn O/ZnO nanocomposites via pyrolysis. *Journal of Solid State Chemistry* **2015,** *230*, 381-389.
40. Delcorte, A.; Leblanc, C.; Poleunis, C.; Hamraoui, K., Computer Simulations of the Sputtering of Metallic, Organic, and Metal–Organic Surfaces with Bi _n and C ₆₀ Projectiles. *The Journal of Physical Chemistry C* **2013,** *117* (6), 2740-2752.
41. De Marco, M. L.; Baaziz, W.; Sharna, S.; Devred, F.; Poleunis, C.; Chevillot-Biraud, A.; Nowak, S.; Haddad, R.; Odziomek, M.; Boissière, C.; others, High-Entropy-Alloy Nanocrystal Based Macro-and Mesoporous Materials. *ACS nano* **2022,** *16* (10), 15837-15849.
42. Aure, M.; Sasaki, M., The Scherrer equation and the dynamical theory of X-ray diffraction research papers. *Acta Cryst* **2016,** *1*, 385-390.
43. Vickerman, J. C.; Briggs, D., *ToF-SIMS: Materials Analysis by Mass Spectrometry*. IM Publications: 2013.
44. Bro, R.; De Jong, S., A fast non-negativity-constrained least squares algorithm. *J. Chemometrics* **1997,** *11* (5), 393-401.
45. Holcomb, G. R.; Tylczak, J.; Carney, C., Oxidation of CoCrFeMnNi high entropy alloys. *Jom* **2015,** *67*, 2326-2339.
46. Cai, Y.; Zhu, L.; Cui, Y.; Geng, K.; Manladan, S. M.; Luo, Z., High-temperature oxidation behavior of FeCoCrNiAlx high-entropy alloy coatings. *Materials Research Express* **2019,** *6* (12), 126552.
47. Anne, B. R.; Shaik, S.; Tanaka, M.; Basu, A., A crucial review on recent updates of oxidation behavior in high entropy alloys. *SN Applied Sciences* **2021,** *3*, 1-23.
48. Kepp, K. P., A quantitative scale of oxophilicity and thiophilicity. *Inorganic Chemistry* **2016,** *55* (18), 9461-9470.

For Table of Contents Only :